LLNL-PROC-687018

Modeling the Detonation Wave Dynamics in Reactive Materials

B. W. White, K. T. Sullivan, A. E. Gash, R. V. Reeves

March 29, 2016

19th International Seminar: New Trends in Research of Energetic Materials
Pardubice, Czech Republic
April 20, 2016 through April 22, 2016

Modeling the Detonation Wave Dynamics in Reactive Materials

Bradley W. White, Kyle T. Sullivan, Alexander E. Gash,
Robert V. Reeves, and H. Keo Springer

Lawrence Livermore National Laboratory, Livermore, CA, USA

white234@llnl.gov

Abstract:

Understanding the effects of shock loading on reactant mixing, ignition, and propagation of reaction fronts in reactive materials is important to the advancement of their use, safety, and performance. In the case of high explosives, controlling detonation pressures and the path of propagation are often of concern for which inert materials may be used for tailoring the response. To better understand the post-ignition wave dynamics in energetic materials under shock loading, we performed simulations using the hydrocode, ALE3D. In these simulations we considered the effects of shock initiation mechanism in TNT with changes in geometry by varying the inert particle (aluminium) loading density, size distribution, and overall particle bed thickness. Particular attention is placed on the disparate material interfaces and interactions of wave fronts with inert materials. We found higher particle loading densities decreases the timing between initiation of the detonation wave and arrival at the bottom surface of the particle bed. Also, particle size had little effect on the average time of arrival across the bottom surface but had larger deviations about the average time of arrival for larger particle sizes.

Keywords: TNT; Ignition and Growth; Detonation Wave; Aluminized Explosive

1 Introduction

At the large scale, it is commonly known that inert materials, such as liners in shaped charges [1-4], can influence the time of arrival of a detonation front along the surface of interest. This has also been observed in line- and plane-wave generators where the geometry itself has an important role in detonation wave-shaping [5-11]. However, less is known about the interactions between an inert particle field and an explosive at the microstructural scale. Since explosives are known to have increased shock sensitivity when the number of hot-spots are increased, which are created by porosity or small inclusions of disparate materials, this has implications on their use, safety, and performance.

There is a renewed interest in understanding the effects of shock loading on reactant mixing, ignition, and self-sustaining propagation of reaction fronts in energetic materials so that their performance may be tailored by modifying the microstructure. In this work, we performed mesoscale simulations that investigate microstructural effects on shock behavior using a two-component energetic system. A high explosive such as TNT mixed with aluminum particles is an ideal candidate for these types of studies with work on this system going back to the 1950's [12]. Aluminum is not only used in other explosives such as PETN [13], Composition B [12,14], TATB [15], but it is used as an additive in propellants to modify their burning behavior [16,17]. Insights gained from this work will directly benefit future work on two-components systems of this type.

2 Calculations

2.1 Modeling Setup

Mesoscale plane strain simulations of TNT infiltrated with a layer of aluminum particles were carried out in ALE3D [18]. Simulations were two-dimensional with a Eulerian mesh of uniform zone size that is 5 μm in both the horizontal and vertical directions. We chose a domain width of 5 mm and a height of 1.5 – 2.5 mm comprised of two layers of TNT. The bottom layer varied in thickness to be 0.5, 1.0, or 1.5mm in height and was infiltrated with varying levels of aluminum particle loading fraction. This left a 1 mm thick layer of pure TNT for the top portion. We then impacted the top layer with an aluminum flyer, 100 μm thick, at an impact speed of 5 km/s to initiate a detonation wave front in TNT. The flyer had the same width as the simulation domain for most simulations discussed in this work. Representative simulation initializations for a 1.0 mm thick particle layer and 50% particle volume fraction are shown on the right-hand side of Figure 1.

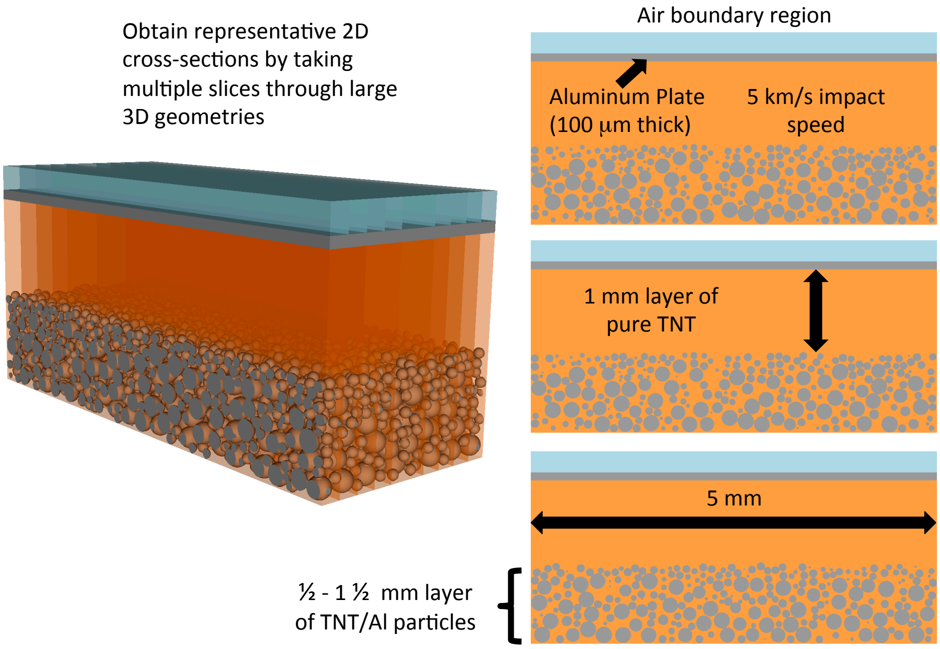

Figure 1: Methodology for initializing simulations and resulting 2D microstructures for plane strain detonation modeling studies.

The top layer of TNT is intentionally left unfilled to allow the detonation front to reach steady-state conditions prior to arriving at the aluminum particle layer. While the flyer velocity initially overdrives the TNT, i.e., impact pressure exceeds C-J pressure of ~ 20 GPa, normal C-J state conditions are achieved in the pure TNT in the first 1 mm. To verify that the pressures decrease to the C-J pressure of TNT, tracer points (gauges) were placed at 0.1 mm height increments within the pure layer. Representative plots of these pressures are shown in Figure 2 where for the first few tracers we see the pressure pulse width and impact pressure resulting from the impacting flyer. Also visible is the gradual decrease in the tracer peak pressures to a magnitude of ~20 GPa as the detonation front progresses further into the TNT layer.

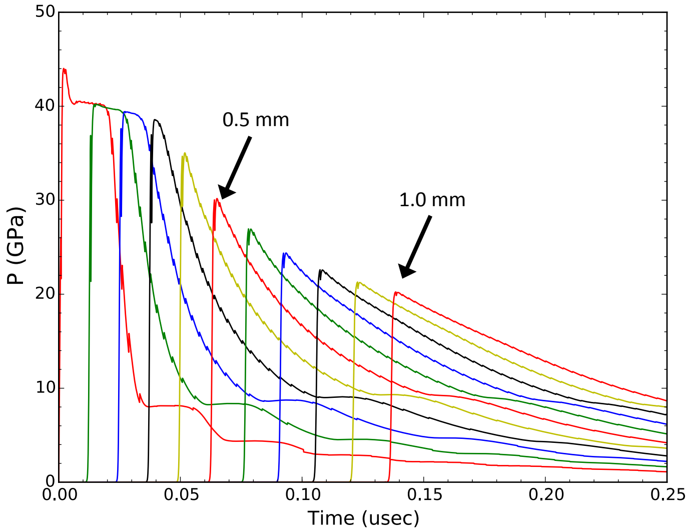

Figure 2: Pressure plots for tracers within a 1 mm run-distance of pure TNT. Peak pressures were found to decrease to near C-J level by 1 mm. For added clarity tracers located at the 0.5 and 1.0 mm run distances are annotated on the plot.

2.1.1 Microstructure Generation of Particle Beds

For the layer consisting of TNT infiltrated with aluminum particles, we generated large 3D regions of particles that were 5.0 mm wide, 2.0 mm deep, and 0.5 to 1.5 mm in height. The particles were randomly distributed within this domain and had a varying bimodal (uniform) particle size distributions and loading fractions. We considered four particle size distributions listed in Table 1 along with the considered volume fractions and layer thickness for those particle sizes. Cross-sections of the 3D particle bed were then used to generate multiple microstructures for studies examining the effects of particles on the detonation wave front and time-of-arrival at the bottom surface (see Figure 1 for an example). For each thickness eight cross sections were taken. By using multiple microstructures we were able to gather statistics on the particles influence by placing tracers gauges to monitor the pressure along the entire bottom surface. In this work the tracers were evenly spaced every 0.1 mm (51 total tracer gauges).

Table 1: Matrix of particle diameters (d_1 and d_2), particle volume fraction (φ_1 and φ_2), total volume fraction (φ_{tot}), and particle bed thickness (t_{pbed}) of simulations carried out in this work.

d_1 / d_2 (µm)	φ_1 / φ_2 (%)	φ_{tot} (%)	t_{pbed} (mm)
50/100	25/25	50	0.5, 1.0, 1.5
60/120	15/15	30	1.0
	20/20	40	1.0
	25/25	50	0.5, 1.0, 1.5
80/160	25/25	50	1.0
100/200	25/25	50	1.0

The aluminum constitutive behavior was modeled using a Steinberg-Guinan strength model [19] and Grüneisen equation of state model (EOS) [19] that had the form:

$$p = \frac{\rho_0 c^2 \mu \left[1 + (1 - \frac{\gamma_0}{2})\mu - \frac{a}{2}\mu^2\right]}{\left[1 - (S_1 - 1)\mu - S_2 \frac{\mu^2}{\mu + 1} - S_3 \frac{\mu^3}{(\mu + 1)^2}\right]^2} + (\gamma_0 + a\mu)E \tag{1}$$

where c is the intercept of the shock velocity-particle velocity (U_s-U_p) curve, S_1, S_2 and S_3 are coefficients of the slope on the U_s-U_p curve, γ_0 is the Grüneisen coefficient and a is the first order volume correction to γ. Additional details regarding the constitutive model for aluminum and parameter values can be found in work by Steinberg et al [19]. Grüneisen EOS parameter values for aluminum are listed in Table 2.

Table 2: Grüneisen equation of state parameters for aluminum. Values taken from [19].

c	S_1	S_2	S_3	γ_0	a	ρ_0
(mm/μs)	(--)	(--)	(--)	(--)	(--)	(g/cm^3)
5.386	1.4	0.0	0.0	1.97	0.48	2.71

2.2 Ignition and Growth Model

For TNT we used the Ignition and Growth reactive flow model [20]. The ignition and growth model uses the Jones-Wilkins-Lee (JWL) EOS model [20] for both the unreacted and reacted explosive, described by:

$$p = A \cdot e^{(-R_1 \cdot V)} + B \cdot e^{(-R_2 \cdot V)} + \omega \cdot C_V \cdot T \tag{2}$$

where p is the pressure, V the relative volume, T the temperature, ω the Grüneisen coefficient, Cv the heat capacity, and A, B, R_1, and R_2 constants which are fitted to Hugoniot and cylinder test data. A three-term equation is used to model the reaction rate of the explosive (see Equation (3)). The first, second, and third terms correspond to the ignition, growth, and completion components, respectively, and contribute to the reaction rate only when the current mass fraction reacted, F, is within a certain range (given to the right of each term). In Equation (3), ρ and ρ_0 correspond to the current and initial density, respectively, p is the pressure, and t is time. The rest of the parameters are constants that are typically fitted to embedded gauge measurements in shock to detonation transition (SDT) experiments and pop-plot data.

$$\frac{dF}{dt} = \begin{cases} I(1-F)^b \left(\frac{\rho}{\rho_0} - 1 - a\right)^x & 0 < F < F_{ig\max} \quad \mathit{Ignition} \\ +G_1 (1-F)^c F^d p^y & 0 < F < F_{G1\max} \quad \mathit{Growth} \\ +G_2 (1-F)^e F^g p^z & F_{G2\min} < F < 1 \quad \mathit{Completion} \end{cases} \tag{3}$$

The unreacted and reacted JWL EOS parameters used in this work to describe TNT are listed in Table 3. The ignition and growth reaction rate parameters are listed in Table 4 for TNT. Both the JWL EOS and ignition and growth reactive flow model parameters were taken from work by J. Kury [21], characterizing the detonation behavior of TNT.

Table 3: Unreacted and Reacted JWL EOS parameters for TNT [21].

JWL Parameter	Unreacted JWL EOS	Product JWL EOS
A (GPa)	17101	3394.889
B (GPa)	-3.745	63.7085
R_1 (--)	9.8	8.3
R_2 (--)	0.98	2.8
ω (--)	0.5675	0.6
C_V (GPa/K)	2.7038e-3	1.0e-3

Table 4: Ignition and Growth reactive flow model parameters for TNT [21]. In addition the parameters below the reference density (ρ_0), energy (E_0), temperature (T_0), shear modulus (μ), and yield strength (σ_y) are given.

Ignition Parameters	Growth Parameters	Completion Parameters
$I = 50.0\ \mu s^{-1}$	$G_1 = 360\ \text{GPa}^{-3}\mu s^{-1}$	$G_2 = 100\ \text{GPa}^{-1}\mu s^{-1}$
$a = 0.0$	$c = 1.0$	$e = 1.0$
$b = 0.667$	$d = 0.667$	$g = 0.111$
$x = 4.0$	$y = 1.2$	$z = 1.0$
$F_{igmax} = 0.03$	$F_{G1max} = 1.0$	$F_{G2min} = 0.0$
$\rho_0 = 1.624$ g/cm^3		
$E_0 = 7.0$ GPa cm^3/ cm^3		
$T_0 = 298$ K		
$\mu = 3.54$ GPa		
$\sigma_y = 0.2$ GPa		

3 Results and Discussion

Prior to arriving at the particle bed, the steady-state detonation wave is planar, as shown in Figure 3 for a pressure plot of a 1.0 mm particle bed thickness and 50/100 μm particle size distribution loaded at 50% volume fraction. At a later time the detonation wave begins to interact with the aluminum particles. Due to differences in shock impedance, this causes wave reflections that result in regions of localized pressure and stagnation. This disrupts the planarity of the detonation wave front and alters the time-of-arrival of the wave at the bottom surface of the particle bed. In regions where the pressure drops within the TNT, the reaction rate decreases as a by-product of the pressure dependent growth and completion terms in the ignition and growth model. Likewise the reaction rates increase in regions of higher pressure. Both of these can alter the velocity of the detonation wave in the particle bed and in particular the TNT downstream from these high-pressure regions.

The pressure within TNT was found in localized regions to be greater than > 30 GPa. When the high-pressure front associated with the detonating TNT or wave reflections reach the aluminum particles, the shock-wave speed can potentially be higher than the detonation speed. For a shock pressure of ~22 GPa the shock velocity in aluminum is ~6.9 km/s [22] which is on order of the detonation velocity of TNT (~6.85 km/s) [21]. For higher shock pressures the shock velocity in aluminum can be much higher than the detonation velocity. This can help to initiate TNT along the particle edges, and often slightly ahead of the main detonation front in the bulk TNT region between the particles.

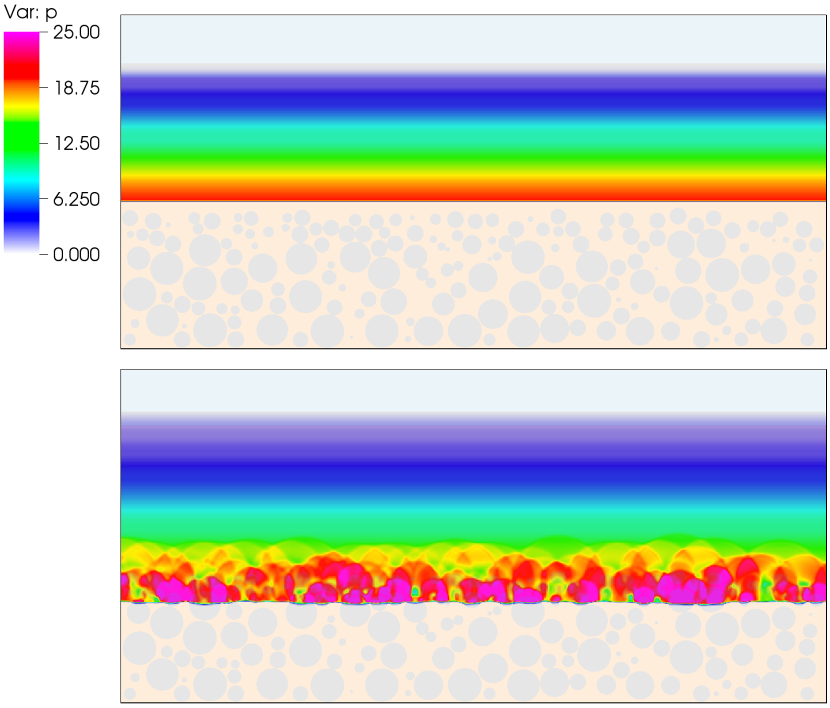

Figure 3: Representative pressure (in GPa) fringe plots, before (top) and after (bottom) the arrival of the detonation wave with the particle bed.

3.1 Effect of Particle Size Distribution

In our analysis of particle size effects we examined four size distributions using a 1 mm thick particle bed. The diameter of the larger particle was set to be equal to 2x the smaller diameter and have equal loading fractions of 25% each (total of 50%). The small particle diameters chosen were, 50, 60, 80, and 100 µm. We then analyzed the tracer data to obtain the average time of arrival and standard deviation for each microstructure (eight for each particle size distribution).

Shown in Figures 4 and 5 are plots with typical times of arrival for different distances across the bottom surface of the particle bed. Figure 4 corresponds to times of arrivals for two different microstructures containing a 60/120 µm particle size distribution, while Figure 5 a 100/200 µm particle size distribution. Also shown on the plots are the average time of arrival and 1st standard deviation as the red line and shaded region, respectively. With changes in particle size we found no significant difference in the average time of arrival. However, with increasing particle sizes there were larger deviations about the average, which is indicative of a much larger deviation from a planar detonation wave front. This can be readily seen in Figure 5 as larger widths for the shaded region than those in Figure 4, as well as in Figure 6, which shows the coefficient of variation ($CV=\sigma_{toa}/\mu_{toa}$) for each of the different small particle diameter chosen for this parameter study.

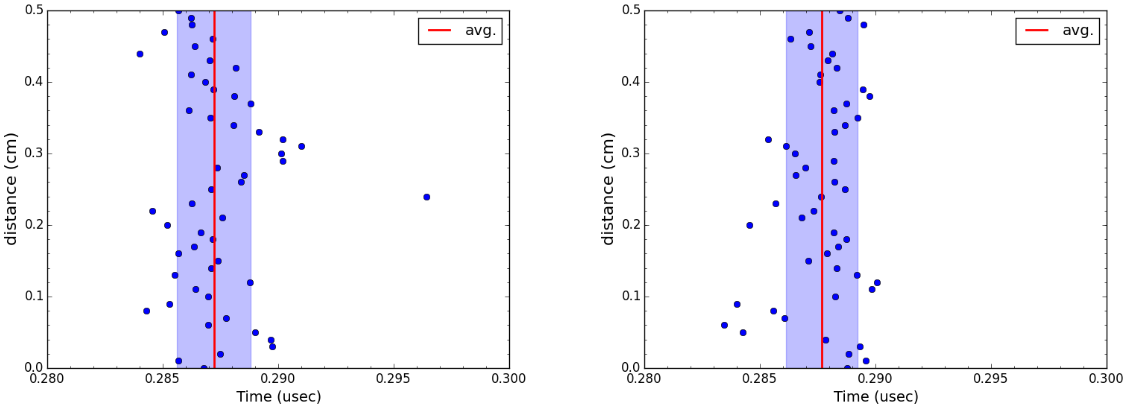

Figure 4: Representative detonation front arrival times across the bottom surface for two individual microstructure samples. Each point corresponds to a different tracer gauge location. Microstructures have 1 mm thick particle beds and a 60/120 μm particle size distribution.

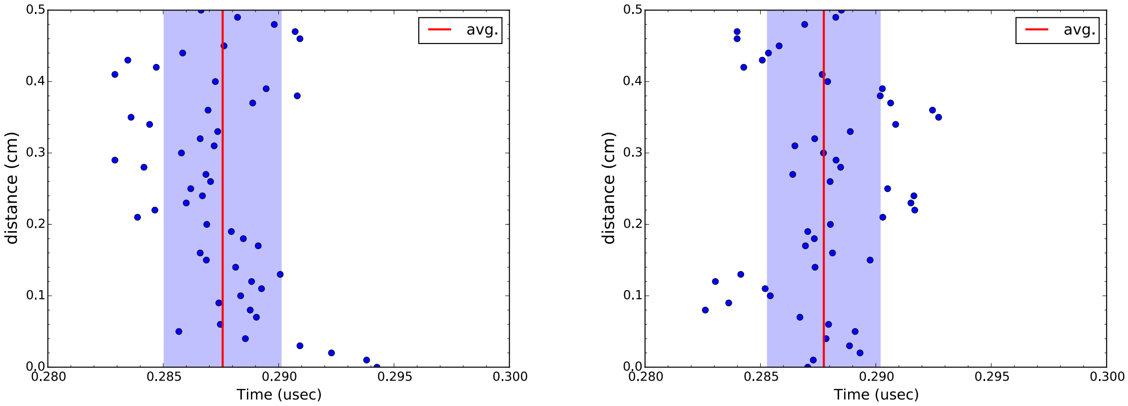

Figure 5: Representative detonation front arrival times across the bottom surface for two individual microstructure samples. Each point corresponds to a different tracer gauge location. Microstructures have 1 mm thick particle beds and a 100/200 μm particle size distribution.

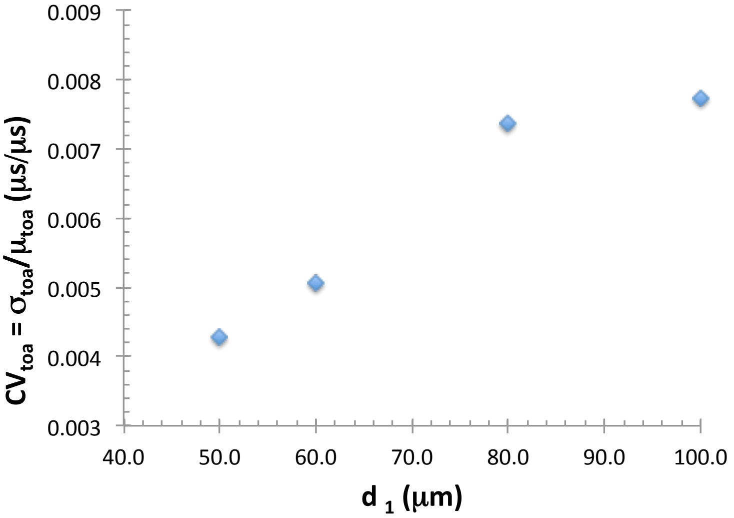

Figure 6: Coefficient of variation ($CV=\sigma_{toa}/\mu_{toa}$) of the arrival time at bottom surface of the 1 mm thick particle bed for the different smaller particle sizes and their associated distributions.

3.2 Effect of Particle Bed Thickness

For a given particle volume fraction of 50%, we vary the thickness of the particle bed for the 50/100mm and 60/120mm particle sizes. We find that the particle size had no noticeable effect on the average time of arrival across the entire bottom surface of the domain. However, there are larger deviations in the time of arrival with increasing particle size regardless of particle bed thickness, which is consistent with our earlier results. Particle bed thickness results are shown in Figures 7 and 8 for average times of arrivals and standard deviations, respectively. A linear fit to the data is found to be $t.o.a = 0.155t_{pbed}+0.133$. When accounting for the thickness of the pure TNT layer, the detonation velocity through both layers is 6.84 – 7.12 km/s. Apart from particle size effects, there are no observable trends in standard deviation with particle bed thickness.

We also performed simulations that remove the particle bed layer to get a baseline for time of arrivals of the detonation wave front. These results are included in Figure 7. We find that without the aluminum particle infiltration, the detonation wave front has longer time of arrivals. Accompanying this is a very slight decrease in pressure, to ~18.5 GPa (for the largest thickness), as the detonation front continued to progress through the pure TNT. This suggests that the presence of the aluminum particles may act to create regions of higher pressure that help sustain the detonation as well as increase the detonation velocity. Our earlier observations support this theory, where shock pressures on the order of the C-J pressure produce shock velocities in the aluminum approximately equal to the detonation velocity of TNT. This also helps initiate TNT along the particle interface and depending on the local variability slightly ahead of the main detonation wave in pure regions.

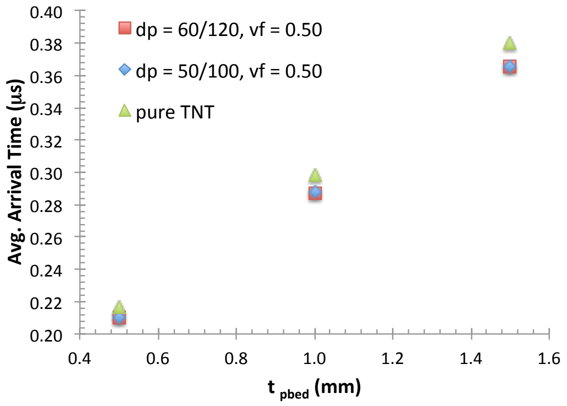

Figure 7: Average detonation front arrival time for different particle bed thicknesses and particle size distributions. Each data point is an average of values from eight microstructures.

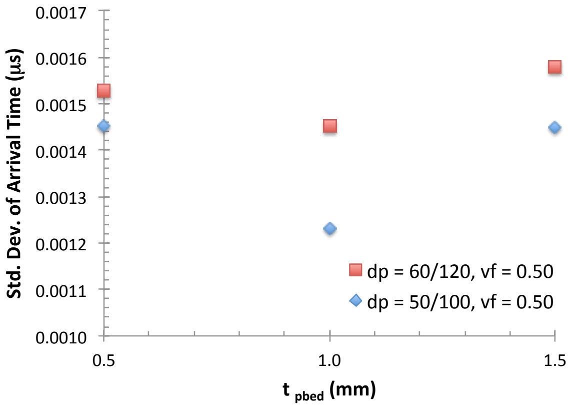

Figure 8: Average standard deviation in arrival time for different particle bed thicknesses and particle size distributions. Each data point is an average of values from eight microstructures.

3.3 Effect of Particle Loading Fraction

As shown in the previous section, particles may act to create regions of higher pressure that help sustain the detonation as well as increase the detonation velocity. We therefore conducted additional studies using a 1 mm thick particle bed and 60/120 μm particle size distribution, that examine the effects of particle loading on the average arrival time. For infiltration levels between 0% and 50% loading, the average time of arrival is found to increase linearly with decreasing levels of particle infiltration, as shown in Figure 9. This reinforces earlier modeling results. However, at higher particle loading fractions, it is more difficult to accurately model a

TNT-aluminum system. As the density of particles is increased, the mean free path between particles decreases. At some critical mean free path, high explosives are unable to sustain a detonation, which may not be captured well with our current macroscopic TNT reactive flow model. This behavior may also depend on additional factors such as the thickness of the particle bed. If the particle bed becomes predominantly aluminum rich there will be more rarefaction waves off the TNT-aluminum interfaces that over a longer period of time may attenuate the pressure. We plan on conducting studies with particle beds thicker than 1.5 mm to investigate this further.

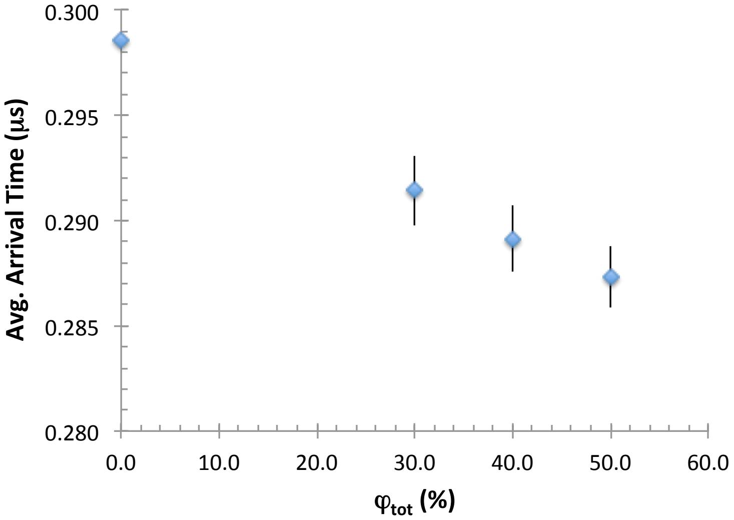

Figure 9: Effect of volume fraction on average time of arrival for a 1 mm thick particle bed and particle size distribution of 60/120 μm.

Acknowledgments

This work performed under the auspices of the U.S. Department of Energy by Lawrence Livermore National Laboratory under Contract DE-AC52-07NA27344. LLNL-PROC-687018.

References

[1] G. Birkhoff, D. P. MacDougall, E. M. Pugh, G. Taylor, "Explosives with lined cavities, *J. App. Phys.*, 19, p. 563-582, 1948.

[2] M. Murphy, K. Weimann, K. Doeringsfeld, J. Speck, "The effect of explosive detonation wave shaping on EFP shape and performance," Proceedings of 13th International Symposium on Ballistics, Stockholm, Sweden, 1992.

[3] W. P. Walters, D. R. Scheffler, "A method to increase the tip velocity of a shaped charge jet" Proceedings of the 23rd International Symposium on Ballistics, Tarragona, Spain, 2007.

[4] M. Ugrčić, and M. Blagojević, "Initiation and correction of the detonation wave in shaped charge peripheral zone" *Scientific Technical Review*, 61(1), p. 17-24, 2011.

[5] W. B. Benedick, "Nitroguanidine explosive plane-wave generator for producing low amplitude shock waves," *Review of Scientific Instruments*, 36, p. 1309-1315, 1965.

[6] J. R. Hearst, L. B. Geesaman, "Uniformity of output from a low-amplitude plane-wave nitroguanidine explosive system," *Lawrence Radiation Laboratory Technical Report UCRL-7877*, 1964.

[7] K. McNesby, G. Sutherland, and R. Benjamin, "Color imaging of shock front emergence in TNT," *Army Research Laboratory Technical Report ARL-TR-6181*, 2012.

[8] J. N. Fritz, “A simple plane-wave explosive lens,” *Los Alamos National Laboratory Technical Report LA-11956-MS*, 1991.

[9] A. M. Frank, and H. H. Chau, “Six-mm, plane-wave shock driver,” *AIP Conference Proceedings*, 309, p. 1651-1654, 1994.

[10] S. A. Weckert, J. Freundt, S. Stojko, “Explosive line wave generators,” *Defense Science and Technology Organisation Technical Note DSTO-TN-1244*, 2013.

[11] J. S. Morris, S. I. Jackson, and L. G. Hill, “A simple line wave generator using commercial explosives,” *AIP Conference Proceedings*, 1195, p. 408-411, 2009.

[12] M. A. Cook, A. S. Filler, R. T. Keyes, W. S. Partridge, and W. O. Ursenbach, “Aluminized explosives,” *The Journal of Physical Chemistry*, 61(2), p. 189-196, 1957.

[13] H. Dong, and S. Zhumei, “Study of the fast reaction characteristics of aluminized PETN explosive powders,” *Combustion and flame* 105(3), p. 428-430, 1996.

[14] Z. Q. Zhou, J. X. Nie, Z. C. Ou, J. F. Qin, and Q. J. Jiao, “Effects of the aluminum content on the shock wave pressure and the acceleration ability of RDX-based aluminized explosives” *Journal of Applied Physics*, 116(14) 144906, 2014.

[15] D. Woody, and J. J. Davis. “The effect of variation of aluminum particle size and polymer on the performance of explosives,” *AIP Conference Proceedings*, 620 p. 942, 2002.

[16] L. Meda, G. Marra, L. Galfetti, F. Severini, and L. De Luca, “Nano-aluminum as energetic material for rocket propellants,” *Materials Science and Engineering: C*, *27*(5), p. 1393-1396, 2007.

[17] A. Dokhan, E. W. Price, J. M. Seitzman, and R. K. Sigman, R. K, “The effects of bimodal aluminum with ultrafine aluminum on the burning rates of solid propellants,” *Proceedings of the Combustion Institute*, *29*(2), p. 2939-2946, 2002.

[18] A. L. Nichols III, “ALE3D User’s Manual, Version 4.26,” *Lawrence Livermore Technical Report LLNL-SM-681737*, 2015.

[19] D. J. Steinberg, S. G. Cochran, and M. W. Guinan, “A constitutive model for metals applicable at high-strain rate” *Journal of Applied Physics*, 51(3) p. 1498, 1980.

[20] E. L. Lee, and C. M. Tarver. “Phenomenological model of shock initiation in heterogeneous explosives,” *Physics of Fluids (1958-1988)*, 23(12), p. 2362-2372, 1980.

[21] J. W. Kury, R. D. Breithaupt, and C. M. Tarver. “Detonation waves in trinitrotoluene." *Shock Waves*, 9(4), p. 227-237, 1999.

[22] S. P. Marsh, *LASL Shock Hugoniot Data*. Vol. 5. Univ of California Press, 1980.